

1 **Re-entrant charge order in overdoped (Bi,Pb)_{2.12}Sr_{1.88}CuO_{6+δ} outside the**
2 **pseudogap regime**

3 Y. Y. Peng^{1†}, R. Fumagalli¹, Y. Ding², M. Minola³, S. Caprara^{4,5}, D. Betto⁶, M. Bluschke³, G. M.
4 De Luca^{7,8}, K. Kummer⁶, E. Lefrançois³, M. Salluzzo⁸, H. Suzuki³, M. Le Tacon⁹, X. J. Zhou²,
5 N. B. Brookes⁶, B. Keimer³, L. Braicovich^{1,6}, M. Grilli^{4,5} and G. Ghiringhelli^{1,10*}

6 **Affiliations:**

7 ¹ Dipartimento di Fisica, Politecnico di Milano, Piazza Leonardo da Vinci 32, I-20133 Milano,
8 Italy.

9 ² Beijing National Laboratory for Condensed Matter Physics, Institute of Physics, Chinese
10 Academy of Sciences, Beijing 100190, China.

11 ³ Max-Planck-Institut für Festkörperforschung, Heisenbergstraße 1, D-70569 Stuttgart, Germany.

12 ⁴ Dipartimento di Fisica, Università di Roma “La Sapienza”, P.le Aldo Moro 5, 00185 Roma,
13 Italy

14 ⁵ CNR-ISC, via dei Taurini, 19 - 00185 Roma, Italy

15 ⁶ ESRF, The European Synchrotron, 71 Avenue des Martyrs, Grenoble, France.

16 ⁷ Dipartimento di Fisica “E. Pancini”, Università di Napoli Federico II, Complesso Monte
17 Sant’Angelo, Via Cinthia 80126 Napoli, Italy

18 ⁸ CNR-SPIN, Complesso MonteSantangelo - Via Cinthia, I-80126 Napoli, Italy.

19 ⁹ Institute of Solid State Physics (IFP), Karlsruhe Institute of Technology, D-76021 Karlsruhe,
20 Germany.

21 ¹⁰ CNR-SPIN, Dipartimento di Fisica, Politecnico di Milano, Piazza Leonardo da Vinci 32, I-
22 20133 Milano, Italy.

23 * Correspondence to: giacomo.ghiringhelli@polimi.it

24 † Present address: Department of Physics and Seitz Materials Research Laboratory, University of
25 Illinois, Urbana, IL 61801, USA

27 **In the underdoped regime, the cuprate high-temperature superconductors exhibit a host of**
28 **unusual collective phenomena, including unconventional spin and charge density**
29 **modulations¹⁻¹², Fermi surface reconstructions, and a pseudogap in various physical**
30 **observables. Conversely, overdoped cuprates are generally regarded as conventional Fermi**
31 **liquids possessing no collective electronic order. In partial contradiction with this widely**
32 **held picture, we report resonant x-ray scattering measurements revealing incommensurate**
33 **charge order reflections for overdoped (Bi,Pb)_{2.12}Sr_{1.88}CuO_{6+δ} (Bi2201), with correlation**
34 **lengths of 40-60 lattice units, that persist up to temperatures of at least 250 K. The**
35 **incommensurate wave vector of the charge order continues the decreasing trend with**
36 **doping already observed in underdoped Bi2201. In overdoped materials, however, charge**
37 **order coexists with a single, unreconstructed Fermi surface without nesting or pseudogap**
38 **features. The discovery of re-entrant charge order in Bi2201 thus calls for investigations in**
39 **other cuprate families and for a reconsideration of theories that posit an essential**
40 **relationship between these phenomena.**

41 High-temperature superconductivity emerges upon doping of holes or electrons into Mott-
42 insulating copper oxides. The strong electronic correlations responsible for Mott localization in
43 the parent compounds generate various competing instabilities in the underdoped regime¹.
44 Although experiments have established charge order (CO) as a universal feature of moderately
45 doped cuprates, its relationship to the ubiquitous “pseudogap” phenomenon has been at the focus
46 of several studies and is still unsettled. Early evidence of charge order had come from La-based
47 cuprates, where charge “stripes” were observed near the doping level $p=1/8$ holes per Cu (refs
48 2,3,4). More recently resonant x-ray scattering (RXS) experiments revealed incommensurate
49 charge order competing with superconductivity also in YBa₂Cu₃O_{6+x} (Y123) and in Hg- and Bi-
50 based cuprates^{5,6,7,8,9,10,11,12}. A detailed comparison of the x-ray data to angle-resolved
51 photoemission spectroscopy (ARPES) data on Bi-based cuprates¹³ suggested that the onset
52 temperature of CO is close to the pseudogap temperature T^* , and that its wave-vector is
53 comparable to the distance between the Fermi arc tips, therefore hinting at a link between CO
54 and the pseudogap in hole-doped systems¹⁴. Also in Y123 the CO onset temperature appears to
55 be always lower than T^* , whereas in electron-doped cuprates CO extends well above T^* , with an
56 onset temperature close to that of the antiferromagnetic (AF) fluctuations, thus suggesting a
57 possible connection between the two¹⁵.

58 The question to what extent CO competes or intertwines with superconductivity remains open,
59 because a crucial aspect of the phenomenology is still missing. When considering the doping p , it
60 is commonly assumed that CO is present only up to the optimal level ($p \leq 0.16$) --- with the
61 possible exception of overdoped $\text{La}_{2-x}\text{Sr}_x\text{CuO}_4$ (La214) where the observation by inelastic
62 neutron scattering of incommensurate spin-order peaks up to $p=0.25$ might be interpreted as
63 indirect evidence of charge density modulations in a “stripe” picture^{16,17}. However, CO has not
64 been directly observed in overdoped La214, and the locking of spin- and charge-modulations at
65 high temperature in this family has been recently questioned¹⁸. On the other hand, various
66 instabilities have been predicted near the Lifshitz point in the overdoped regime^{19,20,21,22}, where a
67 van Hove singularity (vHs) in the electronic density of states moves across the Fermi level and
68 the geometry of the Fermi surface changes from “hole-like” (*i.e.* enclosing a region of empty
69 states centred at the antiferromagnetic point) to “electron-like” (*i.e.* delimiting occupied states
70 around the Γ point). The Bi2201 system is well suited to test these predictions, because the
71 doping level can be tuned over a wide range, well into the overdoped regime and it generates a
72 single Fermi surface, at variance from bilayer compounds showing a double Fermi surface. The
73 single Lifshitz point resulting from this electronic structure greatly facilitates the quantitative
74 correlation between data generated by ARPES and RXS. Additionally, the vHs is particularly
75 strong due to the pronounced 2D character of this system²³ with highly decoupled
76 superconducting planes.

77 Here we present resonant *inelastic* x-ray scattering (RIXS) data that display sharp, intense
78 incommensurate CO diffraction peaks in overdoped Bi2201 over a range of doping levels
79 spanning the Lifshitz point and the endpoint of the superconducting dome. [The continued](#)
80 [decrease of the CO vector with doping points to a picture where charge order would be](#)
81 [ubiquitous across the entire phase diagram. Together with ARPES data on the same samples, our](#)
82 [results provide first experimental evidence at odds with models that posit an essential link](#)
83 [between CO and the pseudogap.](#) We performed RIXS measurements at the Cu L_3 edge on
84 overdoped Bi2201 at four different doping levels (see Methods). We will hereafter use the
85 common notations for the in-plane wave vector \mathbf{Q}_{\parallel} , the pseudo-tetragonal reciprocal lattice units
86 (r.l.u.) $2\pi/a=2\pi/b=1$ (with $a \simeq b \simeq 3.83 \text{ \AA}$), and the reciprocal space indices (H,K,L) . Figure 1a
87 shows the energy/momentum intensity maps for OD11K ($T_c=11\text{K}$, $p \sim 0.215$) along the H
88 direction. The inelastic features in the $[-3,-1]$ eV range, due to inter-orbital transitions (dd

89 excitations)²⁴, depend weakly on momentum, whereas the response centred at zero energy loss
90 exhibits a pronounced maximum at $\mathbf{Q}_{\parallel} = (-0.14, 0)$, shown in Fig. 1c. The RIXS spectrum at $H \simeq$
91 -0.14 r.l.u. (Fig. 1b) is dominated by the elastic peak, which is ~ 20 times more intense than the
92 dd excitations. We found the peak to be elastic within our experimental uncertainty (~ 10 meV),
93 and will refer to this feature as a “resonant *elastic* x-ray scattering” (REXS) peak.

94 Figure 1e shows the Fermi surface (FS) of OD11K measured by ARPES at 20K. We found no
95 replicas of the large Fermi surface, and its shape offers no parallel segments suitable for a good
96 nesting at the CO wave vector $(0.14, 0)$: the shifted FS exhibits a point-like crossing with the
97 original one. In the antinodal region the band lies very close to the Fermi level energy (E_F), with
98 no space for nesting (Fig. 1f). A cut through the FS points separated by \mathbf{Q}_{\parallel} (Fig. 1g) shows no
99 gap opening at E_F , which one would expect in a folded FS due to charge ordering²⁵. On the other
100 hand, a strong van Hove singularity is located slightly below E_F at the M point in the Brillouin
101 zone boundary (Fig. 1h and Supplementary Fig. S7).

102 The REXS peak was found at both positive and negative H with similar intensity, as shown in
103 Fig. 2a, and along both $(1, 0)$ and $(0, 1)$ directions. On the contrary, we could not detect it along
104 the $(1, 1)$ direction (Supplementary Fig. S9), in agreement with prior work on CO in underdoped
105 cuprates^{26,27}. Figure 2b provides the doping dependence of the REXS peak, with cuts along both
106 H and K directions, as indicated by the green cross in Fig. 1d. It is important to note that three
107 doping levels (OD17K, $p \sim 0.205$; OD11K, $p \sim 0.215$; OD0K, $T_c < 2\text{K}$, $p \sim 0.23$) were obtained by
108 post-annealing treatments of the as-grown OD5K ($p \sim 0.225$). Therefore the latter is expected to
109 have a higher degree of structural disorder, as confirmed by the much larger and anisotropic
110 width of the REXS peak and by the broader superconducting transition (Supplementary Fig.
111 S1a); moreover, the Q_{CO} of OD5K falls out of the trend set by the three other samples.

112 To assess that the REXS peak arises from charge order, we have exploited the polarimeter of our
113 RIXS facility²⁸. Spin-related scattering implies a 90° rotation of the photon polarization²⁹,
114 whereas pure charge scattering, without spin-flip excitations, necessarily conserves the photon
115 polarization. As shown in Fig. 2c, the REXS peak is purely polarization-conserving. To clarify
116 whether the peak originates from a modulation of the valence electron charge density, we
117 checked its resonant behaviour, since a charge density modulation is detectable only at resonance
118 at our photon energy, whereas a generic lattice superstructure would be visible also off-

119 resonance³⁰. Figure 3a shows the incident photon energy dependence of the REXS peak, which
120 closely resembles the spectra of the Cu L_3 x-ray absorption spectrum (XAS). Unlike YBCO,
121 which has two inequivalent Cu sites contributing to the XAS spectra⁶, in Bi2201 the Cu L_3
122 absorption peak is fully due to the Cu in the CuO₂ planes, and the strictly resonant peak can thus
123 be unequivocally assigned to modulations of the charge density in the CuO₂ planes. While the
124 REXS peak intensity decreases upon detuning from the resonance, its position and width are
125 unchanged (Figure 3b). This photon energy dependence is identical to the resonance of CO in
126 underdoped Bi2201 (ref. 13).

127 Figure 3c shows the temperature dependence of the REXS peak in OD11K. Although the peak
128 broadens slightly as the temperature is raised, its integrated intensity is almost temperature
129 independent up to 250K (Fig. 3d), indicating that the onset of charge order occurs well above
130 250K. Since T^* of OD11K is approximately zero³¹, as confirmed by the absence of gap at the
131 antinode at 20K (Fig. 1f), this means that the REXS peak is present in the absence of the
132 pseudogap. [The very small temperature dependence is confirmed by energy-integrated resonant
133 x-ray scattering measurements, carried out on the OD17K sample \(Fig. 3d and Supplementary
134 Fig. S10\), and showing that the REXS peak is invariant across \$T_c\$, similarly to the CO behaviour
135 in underdoped Bi2201 \(ref. 13\).](#) It is noteworthy that the competition between CO and
136 superconductivity in the underdoped cuprates varies. While the CO is found to compete
137 prominently with SC in underdoped Y123 (refs 6-10) and La214 (ref. 32), this behaviour is less
138 evident in Bi₂Sr₂CaCu₂O_{8+ δ} (ref. 33), Bi2201 (refs 13, 27) and HgBa₂CuO_{4+ δ} (refs 34, 35).

139 Figures 4a to c present an overview of the wave vector of the REXS peak, Q_{CO} , as well as its
140 correlation length and its integrated intensity (“volume”) as functions of doping, including earlier
141 data on underdoped Bi2201 (refs 13,27). The newly discovered Q_{CO} is approximately half of that
142 of the underdoped samples, extending the known negative slope of $Q_{CO}(p)$ to the overdoped
143 region. As already mentioned, the peak intensity (normalized to the dd excitations) is much
144 higher in the overdoped samples. This is combined with a much smaller width in Q-space: the
145 charge order is rather long-ranged in the overdoped region, with the only exception of the as-
146 grown OD5K whose REXS peak is relatively weak and broad. In the three other overdoped
147 samples the correlation lengths $\xi_{H,K}$ are in the range of $40a$ to $60a$, an order of magnitude larger
148 than those of underdoped Bi2201 ($\sim 6a$). It is noteworthy that this long-range correlation of

149 charge order is comparable with the stripe-order in $\text{La}_{1.875}\text{Ba}_{0.125}\text{CuO}_4$ (refs 2,3,4) and the field-
150 induced CO in YBCO (refs 9,10). Interestingly, the integrated intensity of the REXS peak (see
151 Methods) also shows two comparable maxima, one around $p \sim 0.115$ and one around $p \sim 0.215$.
152 Figure 4d shows the extended phase diagram of charge order in Bi2201, including also the
153 checkerboard-like charge order that was observed by scanning tunnelling microscopy (STM)
154 from the insulating state ($p \simeq 0.07$)³⁶ up to OD15K ($p \simeq 0.21$)³⁷, and characterized by a doping-
155 independent $Q_{\text{CO}} \sim 0.25$ r.l.u.. On the other hand, RXS measurements revealed a short-ranged CO
156 in the pseudogap state up to optimal doping, and a long-ranged CO, with small T -dependence
157 between 20 K and 250K, outside the pseudogap region up to $p \simeq 0.23$. Given the different charge
158 order wave vectors determined from STM and RXS, their relations remain to be further studied.
159 The schematic Fermi surfaces of Bi2201 at three selected dopings ($p \simeq 0.11, 0.16$ and 0.22) are
160 shown on the top panels. A hole-like Fermi surface is observed in a broad doping range; it grows
161 in size with doping and breaks into Fermi arcs below T^* (refs 38,39). It eventually transforms
162 into an electron-like FS in the case of OD0K, where the Lifshitz transition takes place in Bi2201
163 (ref. 39).

164 Our discovery encourages reconsidering the charge ordering phenomenon and, with it, a
165 reassessing the theoretical models proposed so far. In particular, as spin instabilities have been
166 reported only close to the Mott-insulating state, they are unlikely the cause of CO in the
167 overdoped regime, where the van Hove singularity seems more relevant^{19,20,21,22}. However, the
168 instabilities related to the vHs are typically associated with nesting features of the Fermi surface
169 that are absent in our experiments. Looking for an appealing common scenario for CO in
170 underdoped and overdoped regions, we consider the “frustrated phase separation” approach (see
171 Methods and Supplementary Information), previously proposed for the underdoped
172 regime^{40,41,42,43}, in which some generic (phononic and/or magnetic) *non-critical* effective
173 attraction drives the system towards electronic phase separation. As the segregation of charges
174 over large regions is prevented by the electron-electron Coulomb repulsion, the system finds a
175 compromise by forming a CO state where charge is segregated on a short length scale while
176 large-scale charge neutrality is maintained. This mechanism accounts for a ubiquitous tendency
177 towards CO with a wave vector that is not tied to nesting features of the Fermi surface. It also
178 accounts for a re-entrancy of charge order, because the propensity to this instability depends on

179 the electronic density of states which exhibits two maxima as a function of doping
180 (Supplementary Fig. S12). The first maximum at low doping is due to narrowing of the
181 conduction band induced by electronic correlations, and at high doping the vHs generates a
182 second maximum.

183 In contrast to theories ascribing charge orders to antiferromagnetic correlations in the pseudogap
184 phase, which are applicable only to the underdoped region^{44,45,46}, and to those that attribute
185 charge instabilities only to the vHs, which are not relevant for CO in underdoped cuprates²⁰, we
186 are suggesting here a unified scenario for the entire phase diagram. We note that alternative
187 schemes^{21,22} that rely on Fermi surface folding or nesting are difficult to reconcile with our
188 ARPES results. Future work to address the detailed structural and electronic textures of the CO
189 state in Bi2201 is required to reveal the universality of CO in the overdoped regime. Though the
190 vHs is generally observed in cuprates, its position and extent in momentum space strongly vary
191 among families⁴⁷. The study of other highly 2D compounds such as the single-layer TI-based
192 cuprates can validate our interpretation. In any case, our discovery of a strong electronic
193 instability in the overdoped regime invites investigating the commonalities and differences of
194 cuprates across the optimal doping level and the nearby quantum critical points.

195

196

197 **Methods**

198 **Sample characterisation**

199 Single crystals of $(\text{Bi,Pb})_{2.12}\text{Sr}_{1.88}\text{CuO}_{6+\delta}$ are grown by the travelling solvent floating zone
200 method. The sample growth and characterization methods have been reported previously⁴⁸. The
201 as-grown single crystals with nominal composition $\text{Pb}_{0.25}\text{Bi}_{1.87}\text{Sr}_{1.88}\text{CuO}_{6+\delta}$ were post-annealed
202 in different atmospheres including vacuum and high pressured oxygen at different temperatures
203 ($500^{\circ}\text{C} \sim 600^{\circ}\text{C}$) in order to adjust the doping level to change T_c and to make the samples
204 homogeneous. Supplementary Figure S1 shows the temperature dependence of magnetization for
205 as-grown Bi2201 single crystals and for samples after various annealing processes. The as-grown
206 OD5K showed a broad transition width of more than 3K. After annealing, the magnetization of
207 OD17K and OD11K showed a sharp transition width $\sim 1\text{K}$. The OD0K showed no

208 superconducting transition down to 2K, which was the minimum temperature of our apparatus,
209 thus we indexed it as OD0K.

210

211 **ARPES measurements**

212 The ARPES measurements were carried out on the angle-resolved photoemission system with a
213 Helium discharge lamp in the Institute of Physics, Chinese Academy of Sciences, China. The
214 photon energy was 21.218 eV and the energy resolution was set to 10 meV, and the angular
215 resolution was 0.3 degree. The samples were cleaved *in situ* and measured under ultrahigh
216 vacuum, pressure lower than 6×10^{-11} mbar. The Fermi level is referenced by measuring on the
217 Fermi edge of a clean polycrystalline gold that is electrically connected to the sample.

218

219 **RIXS and RXS measurements**

220 The RIXS measurements were performed at the ID32 beamline of ESRF (The European
221 Synchrotron, France) using the new high-resolution ERIXS spectrometer. The resonant
222 conditions were achieved by tuning the energy of the incident x-ray to the maximum of the Cu L_3
223 absorption peak, around 931 eV. The total instrumental energy resolution was set at 65 meV,
224 determined as FWHM of the non-resonant diffuse scattering from the silver paint. The samples
225 were cleaved out-of-vacuum to expose a fresh surface. The XAS measurements were made at the
226 ID32 of ESRF. The RIXS experimental geometry is shown in Supplementary Fig. S5. X-rays are
227 incident on the sample surface and scattered by an angle 2θ . Reciprocal lattice units (r.l.u.) were
228 defined by using the pseudo-tetragonal unit cell with $a = b = 3.83 \text{ \AA}$ and $c = 24.54 \text{ \AA}$, where the
229 axis c is normal to the cleaved sample surface. The sample can be rotated azimuthally around the
230 c axis to choose the in-plane wave vector component. Data in the text were taken with $2\theta = 149^\circ$,
231 giving $|\mathbf{Q}| = 0.85 \text{ \AA}^{-1}$, which allows one to cover the whole first Brillouin zone along the [100]
232 direction ($\sim 0.82 \text{ \AA}^{-1}$). Here, the negative (positive) Q_{\parallel} corresponds to grazing-incidence (grazing-
233 emission) geometry. For $Q_{\text{Co}} \sim 0.09\text{-}0.14$ r.l.u., the L values correspond to 3.5-3.44 r.l.u.. Each
234 RIXS spectrum was measured for 1 minute (sum of individual spectra of 5 seconds). The quasi-
235 elastic intensity was determined by the integral of 0 ± 0.1 eV. That intensity was normalized to
236 the integral of dd excitations in the RIXS spectrum between 1 and 3 eV energy loss. For the
237 polarimeter measurements, the spectrum without polarimeter was measured for 15 min and the

238 spectrum with polarimeter was measured for 50 min. The total instrumental energy resolution
239 was set at ~ 100 meV. The integrated intensity of the REXS peak is proportional to
240 $\xi_H^{-1} \times \xi_K^{-1} \times d$, where d is the height of the REXS peak after subtracting the background from
241 the curves of Fig. 2b.

242

243 The energy-integrated resonant x-ray scattering (RXS) measurements were performed at the
244 UE46-PGM1 beamline at the BESSY II synchrotron of the Helmholtz-Zentrum-Berlin. The
245 geometry was identical to that of the RIXS experiment. We used linearly polarized incident light
246 perpendicular to the scattering plane (σ -polarization). The sample was mounted inside an ultra-
247 high-vacuum two-circle diffractometer and directly onto the cold finger of a liquid-Helium-flow
248 cryostat, allowing lower base temperature (~ 10 K) than the RIXS setup and, thus, measurements
249 below T_c for the OD17K sample. The scattered photons were detected using a standard
250 photodiode without discrimination of both polarization and energy, implying that the measured
251 intensities represent an integration over all elastic and inelastic scattering processes.

252

253 **The theoretical model and calculations**

254 Our theoretical approach is based on a Fermi liquid scheme (details in Supplementary
255 Information), which is the standard description of the metallic state. In this framework, the
256 effects of CO with wavevector \mathbf{Q} are described by the charge susceptibility in the customary
257 Random Phase Approximation (RPA). A charge instability at a given wave vector \mathbf{Q}_{co} is
258 obtained by a diverging charge susceptibility. The instability conditions are realized by a large
259 density of states (DOS) in two different regimes of phase diagram: while in the overdoped region
260 the strong vHs directly provides the required large DOS, below optimal doping the substantial
261 electron-electron correlation raises the effective electron mass m^* and, consequently, the
262 quasiparticle DOS (ref.49). Therefore the bare single-particle susceptibility given by the
263 Lindhard polarization function does not provide the instability conditions at its peak value. The
264 above description of the CO instability has a mean-field character and it does not include the
265 effect of the CO fluctuations. These are then considered within a standard Ginzburg-Landau
266 approach describing the effects of fluctuations in spoiling the long-rang CO state and leaving the
267 CO with a finite correlation length.

268

269 **Acknowledgments**

270 This work was supported by ERC-P-ReXS project (2016-0790) of the Fondazione CARIPLO
271 and Regione Lombardia, in Italy. M. M. was partially supported by the Alexander von Humboldt
272 Foundation. XJZ thanks financial support from the National Natural Science Foundation of
273 China (11334010 and 11534007), the National Key Research and Development Program of
274 China (2016YFA0300300) and the Strategic Priority Research Program (B) of Chinese Academy
275 of Sciences (XDB07020300). SC and MG acknowledge financial support from the Sapienza
276 University Project No. C26A115HTN. The authors acknowledge insightful discussions with
277 T. P. Devereaux, S. Kivelson, C. Di Castro, B. Moritz, P. Abbamonte and W. Metzner. [The](#)
278 [authors acknowledge the help of S. Sun and P. Abbamonte for the x-ray diffraction](#)
279 [measurements, collected at Department of Physics and Seitz Materials Research Laboratory,](#)
280 [University of Illinois, USA, the assistance of E. Schierle for the RXS measurements at BESSY II](#)
281 [\(HZB\) is gratefully acknowledged and of M. Celebrano for the AFM images acquired at the](#)
282 [Physics Department of the Politecnico di Milano.](#) The RIXS experimental data were collected at
283 the beam line ID32 of the European Synchrotron (ESRF) in Grenoble (F) using the ERIXS
284 spectrometer designed jointly by the ESRF and Politecnico di Milano.

285

286 **Author contributions**

287 G.G., Y.Y.P. and L.B. conceived and designed the experiments with suggestions from M.M.,
288 N.B.B. and B.K.; Y.Y.P., R.F., G.G., L.B., M.M., D.B., G.M.D.L., K.K., E.L., M.S., H.S. and
289 N.B.B. performed the RIXS measurements; [M.M., R.F. and M.B performed the RXS](#)
290 [measurements; G.G. contributed to AFM measurements;](#) Y.D. and X.J.Z. performed the ARPES
291 measurements. Y.Y.P. and G.G. analysed the RIXS experimental data; Y.Y.P., Y.D. and X.J.Z.
292 analysed the ARPES experimental data; M.G. and S.C. performed the theoretical calculations;
293 Y.D. and X.J.Z. synthesized, grew and characterized the Bi2201 single-crystals. Y.Y.P., G.G.,
294 B.K., and M.G. wrote the manuscript with the input from L.B., M.L.T., M.M. and R.F., and
295 contributions from all authors.

296

297 **Competing financial interests**

298 The authors declare no competing financial interests.

299

300 **References and Notes:**

-
- ¹ Keimer, B., Kivelson, S. A., Norman, M. R., Uchida, S., Zaanen, J. From quantum matter to high-temperature superconductivity in copper oxides. *Nature* **518**, 179 (2015).
 - ² Tranquada, J. M., Sternlieb, B. J., Axe, J. D., Nakamura, Y., Uchida, S. Evidence for stripe correlations of spins and holes in copper oxide superconductors. *Nature* **375**, 561 (1995).
 - ³ Fujita, M., Goka, H., Yamada, K., Matsuda, M. Competition between Charge- and Spin-Density-Wave Order and Superconductivity in $\text{La}_{1.875}\text{Ba}_{0.125-x}\text{Sr}_x\text{CuO}_4$. *Phys. Rev. Lett.* **88**, 167008 (2002).
 - ⁴ Abbamonte, P. *et al.* Spatially modulated 'Mottness' in $\text{La}_{2-x}\text{Ba}_x\text{CuO}_4$. *Nat. Phys.* **1**, 155 (2005).
 - ⁵ Wu, T. *et al.* Magnetic-field-induced charge-stripe order in the high-temperature superconductor $\text{YBa}_2\text{Cu}_3\text{O}_y$. *Nature* **477**, 191-194 (2011).
 - ⁶ Ghiringhelli, G. *et al.* Long-Range Incommensurate Charge Fluctuations in $(\text{Y,Nd})\text{Ba}_2\text{Cu}_3\text{O}_{6+x}$. *Science* **337**, 821 (2012).
 - ⁷ Chang, J. *et al.* Direct observation of competition between superconductivity and charge density wave order in $\text{YBa}_2\text{Cu}_3\text{O}_{6.67}$. *Nat. Phys.* **8**, 871 (2012).
 - ⁸ Blanco-Canosa, S. *et al.* Resonant x-ray scattering study of charge-density wave correlations in $\text{YBa}_2\text{Cu}_3\text{O}_{6+x}$. *Phys. Rev. B* **90**, 054513 (2014).
 - ⁹ Gerber, S. *et al.* Three-dimensional charge density wave order in $\text{YBa}_2\text{Cu}_3\text{O}_{6.67}$ at high magnetic fields. *Science* **350**, 949 (2015).
 - ¹⁰ Chang, J. *et al.* Magnetic field controlled charge density wave coupling in underdoped $\text{YBa}_2\text{Cu}_3\text{O}_{6+x}$. *Nat. Commun.* **7**, 11494 (2016).
 - ¹¹ Tabis, W. *et al.* Charge order and its connection with Fermi-liquid charge transport in a pristine high-Tc cuprate. *Nat. Commun.* **5**, 5875 (2014).
 - ¹² Hashimoto, M. *et al.* Direct observation of bulk charge modulations in optimally doped $\text{Bi}_{1.5}\text{Pb}_{0.6}\text{Sr}_{1.54}\text{CaCu}_2\text{O}_{8+\delta}$. *Phys. Rev. B* **89**, 220511(R) (2014).
 - ¹³ Comin, R. *et al.* Charge order driven by fermi-arc instability in $\text{Bi}_2\text{Sr}_{2-x}\text{La}_x\text{CuO}_{6+\delta}$. *Science* **343**, 390 (2014).
 - ¹⁴ Allais, A., Chowdhury, D. and Sachdev, S. Connecting high-field quantum oscillations to zero-field electron spectral functions in the underdoped cuprates. *Nat. Commun.* **5**, 5771 (2014).
 - ¹⁵ da Silva Neto, E. H. *et al.* Doping-dependent charge order correlations in electron-doped cuprates. *Sci. Adv.* **2**, 1600782 (2016).
 - ¹⁶ Tranquada, J. M. *et al.* Coexistence of, and Competition between, Superconductivity and Charge-Stripe Order in $\text{La}_{1.6-x}\text{Nd}_{0.4}\text{Sr}_x\text{CuO}_4$. *Phys Rev. Lett.* **78**, 338 (1997).
 - ¹⁷ Yamada, K. *et al.* Doping dependence of the spatially modulated dynamical spin correlations and the superconducting-transition temperature in $\text{La}_{2-x}\text{Sr}_x\text{CuO}_4$. *Phys. Rev. B* **57**, 6165 (1998).

-
- ¹⁸ Miao, H. et al High-temperature charge density wave correlations in $\text{La}_{1.875}\text{Ba}_{0.125}\text{CuO}_4$ without spin-charge locking, *PNAS* 1708549114 (2017).
- ¹⁹ Zanchi, D. and Schulz, H. J. Superconducting instabilities of the non-half-filled Hubbard model in two dimensions. *Phys. Rev. B* **54**, 9509 (1996).
- ²⁰ Gonzalez, J. Charge instabilities near a Van Hove singularity. *Phys. Rev. B* **63**, 045114 (2001).
- ²¹ Holder, T. and Metzner, W., Incommensurate nematic fluctuations in two-dimensional metals. *Phys. Rev. B* **85**, 165130 (2012).
- ²² Bulut, S., Atkinson, W. A., and Kampf, A. P. Spatially modulated electronic nematicity in the three-band model of cuprate superconductors. *Phys. Rev. B* **88**, 155132 (2013).
- ²³ King, D.M. et al, Observation of a Saddle-Point Singularity in $\text{Bi}_2(\text{Sr}_{0.97}\text{Pr}_{0.03})_2\text{CuO}_{6+\delta}$ and Its Implications for Normal and Superconducting State Properties *Phys Rev. Lett.* **73**, 3298 (1994).
- ²⁴ Moretti Sala, M. *et al.* Energy and symmetry of *dd* excitations in undoped layered cuprates measured by $\text{Cu } L_3$ resonant inelastic x-ray scattering. *New J. Phys.* **13**, 043026 (2011).
- ²⁵ Chen, C.-W., Choe, J., Morosan, E. Charge density waves in strongly correlated electron systems. *Rep. Prog. Phys.* **79**, 084505 (2016).
- ²⁶ Comin, R. *et al.* Symmetry of charge order in cuprates. *Nat. Mater.* **14**, 796 (2015).
- ²⁷ Peng, Y. Y. *et al.* Direct observation of charge order in underdoped and optimally doped $\text{Bi}_2(\text{Sr},\text{La})_2\text{CuO}_{6+\delta}$ by resonant inelastic x-ray scattering. *Phys. Rev. B* **94**, 184511 (2016).
- ²⁸ Braicovich, L. *et al.* The simultaneous measurement of energy and linear polarization of the scattered radiation in resonant inelastic soft x-ray scattering. *Rev. Sci. Instrum.* **85**, 115104 (2014).
- ²⁹ Ament, L. J. P., Ghiringhelli, G., Moretti Sala, M., Braicovich, L. & van den Brink, J. Theoretical Demonstration of How the Dispersion of magnetic excitations in cuprate compounds can be determined using resonant inelastic X-ray scattering. *Phys. Rev. Lett.* **103**, 117003 (2009).
- ³⁰ Abbamonte, P., Charge modulations versus strain waves in resonant x-ray scattering. *Phys. Rev. B* **74**, 195113 (2006).
- ³¹ Kawasaki, S. J. *et al.* Carrier-concentration dependence of the pseudogap ground state of superconducting $\text{Bi}_2\text{Sr}_{2-x}\text{La}_x\text{CuO}_{6+\delta}$ revealed by $^{63,65}\text{Cu}$ -nuclear magnetic resonance in very high magnetic fields *Phys. Rev. Lett.* **105**, 137002 (2010).
- ³² Croft, T. P., Lester, C., Senn, M. S., Bombardi, A., and Hayden, S. M. Charge density wave fluctuations in $\text{La}_{2-x}\text{Sr}_x\text{CuO}_4$ and their competition with superconductivity. *Phys. Rev. B* **89**, 224513 (2014).
- ³³ da Silva Neto, E. H. et al. Ubiquitous Interplay Between Charge Ordering and High-Temperature Superconductivity in Cuprates. *Science* **343**, 393 (2014).
- ³⁴ Tabis, W. *et al.* Synchrotron x-ray scattering study of charge-density-wave order in $\text{HgBa}_2\text{CuO}_{4+\delta}$. *Phys. Rev. B* **96**, 134510 (2017).
- ³⁵ Campi, G. et al. Inhomogeneity of charge-density-wave order and quenched disorder in a high-Tc superconductor. *Nature* **525**, 359 (2015).

-
- ³⁶ Cai, P. *et al.* Visualizing the evolution from the Mott insulator to a charge-ordered insulator in lightly doped cuprates. *Nat. Phys.* **12**, 1047 (2016).
- ³⁷ He, Y. *et al.* Fermi Surface and pseudogap evolution in a cuprate superconductor. *Science* **344**, 608 (2014).
- ³⁸ Meng, J. Q. *et al.* Coexistence of Fermi arcs and Fermi pockets in a high-Tc copper oxide superconductor. *Nature* **462**, 335 (2009).
- ³⁹ Kondo, T. *et al.* Hole-concentration dependence of band structure in $(\text{Bi, Pb})_2(\text{Sr, La})_2\text{CuO}_{6+\delta}$ determined by the angle-resolved photoemission spectroscopy. *J. Electron Spectrosc. Relat. Phenom.* **137**, 663-668 (2004).
- ⁴⁰ Emery, V.J., Kivelson, S.A. Frustrated electronic phase separation and high-temperature superconductors. *Physica C: Supercond.* **209**, 597 (1993).
- ⁴¹ Castellani, C., Di Castro, C., Grilli, M. Singular Quasiparticle Scattering in the Proximity of Charge Instabilities. *Phys. Rev. Lett.* **75**, 4650 (1995).
- ⁴² Andergassen, S., Caprara, S., Di Castro, C., Grilli, M. Anomalous Isotopic Effect Near the Charge Ordering Quantum Criticality. *Phys. Rev. Lett.* **87**, 056401 (2001).
- ⁴³ Caprara, S., Di Castro, C., Seibold, G., Grilli, M., Dynamical charge density waves rule the phase diagram of cuprates. *Phys. Rev. B* **95**, 224511 (2017).
- ⁴⁴ Metlitski, M. A. and Sachdev, S. Quantum phase transitions of metals in two spatial dimensions. II. Spin density wave order. *Phys. Rev. B* **82**, 075128 (2010).
- ⁴⁵ Efetov, K. B., Meier, H., and Pépin, C. Pseudogap state near a quantum critical point. *Nat. Phys.* **9**, 442 (2013).
- ⁴⁶ Wang, Y. and Chubukov, A. Charge-density-wave order with momentum $(2Q,0)$ and $(0,2Q)$ within the spin-fermion model: Continuous and discrete symmetry breaking, preemptive composite order, and relation to pseudogap in hole-doped cuprates. *Phys. Rev. B* **90**, 035149 (2014).
- ⁴⁷ Markiewicz, R. S. A survey of the van Hove scenario for high-Tc superconductivity with special emphasis on pseudogaps and striped phases. *J. Phys. Chem. Sol.* **58**, 1179 (1997).
- ⁴⁸ Zhao, L. *et al.* High-quality large-sized single crystals of Pb-doped $\text{Bi}_2\text{Sr}_2\text{CuO}_{6+\delta}$ high-Tc superconductors grown with traveling solvent floating zone method. *Chin. Phys. Lett.* **27**, 087401 (2010).
- ⁴⁹ Kotliar, G. and Ruckenstein, A.E., New Functional Integral Approach to Strongly Correlated Fermi Systems: The Gutzwiller Approximation as a Saddle Point. *Phys Rev. Lett.* **57**, 1362 (1986).

Figures

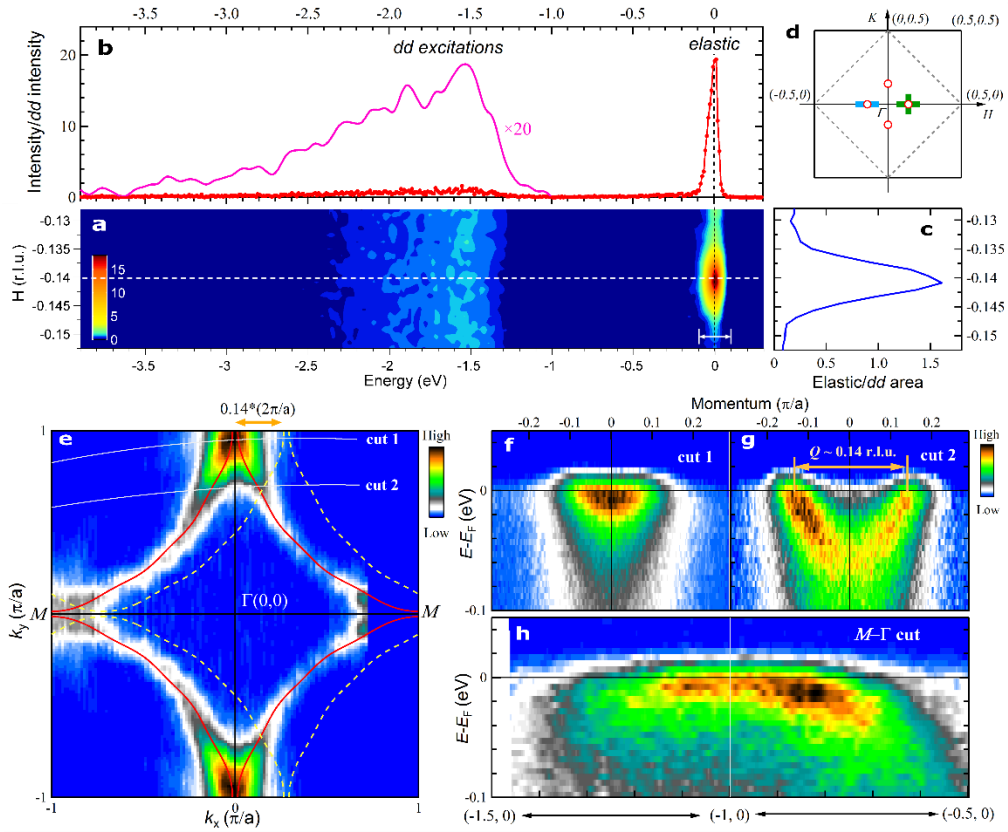


Figure 1: Observation of a quasi-elastic peak by RIXS in overdoped $(\text{Bi,Pb})_{2.12}\text{Sr}_{1.88}\text{CuO}_{6+\delta}$ ($T_c=11\text{K}$, $p\sim 0.215$). **a**, Energy/momentum intensity map of RIXS spectra along the $(-0.5, 0) - (0, 0)$ symmetry direction, indicated by the thick blue line in panel **(d)**. The data were taken with σ -polarized incident light at 20K. The RIXS spectrum at $H \approx -0.14$ r.l.u. indicated by the white dashed line is shown in **(b)**. The dd excitations are shown additionally after smoothing and multiplied by 20 to be comparable to the elastic peak. **c**, The quasielastic RIXS intensity is given by the integral around $E \sim 0$, as indicated in **(a)**. **d**, Reciprocal-space image. The hollow red circles indicate the observed quasi-elastic peak. **e**, Photoemission intensity at the Fermi energy (E_F) as a function of momenta k_x and k_y for OD11K at 20K. It is obtained by integrating within a $(-10 \text{ meV}, 10 \text{ meV})$ energy window and symmetrizing the original data with respect to the $(-\pi/a, 0) - (\pi/a, 0)$ line. The red lines, obtained by tight-binding fitting to the data, serve as a guide to the eyes. The dashed yellow lines indicate the Fermi surface shifted horizontally by $Q_{\text{Co}} \approx 0.14$ r.l.u.. **f, g**, Electronic dispersions for the cuts (indicated by the white lines in **e**). **h**, Electronic dispersion for the cut along M - Γ direction near the Brillouin zone boundary.

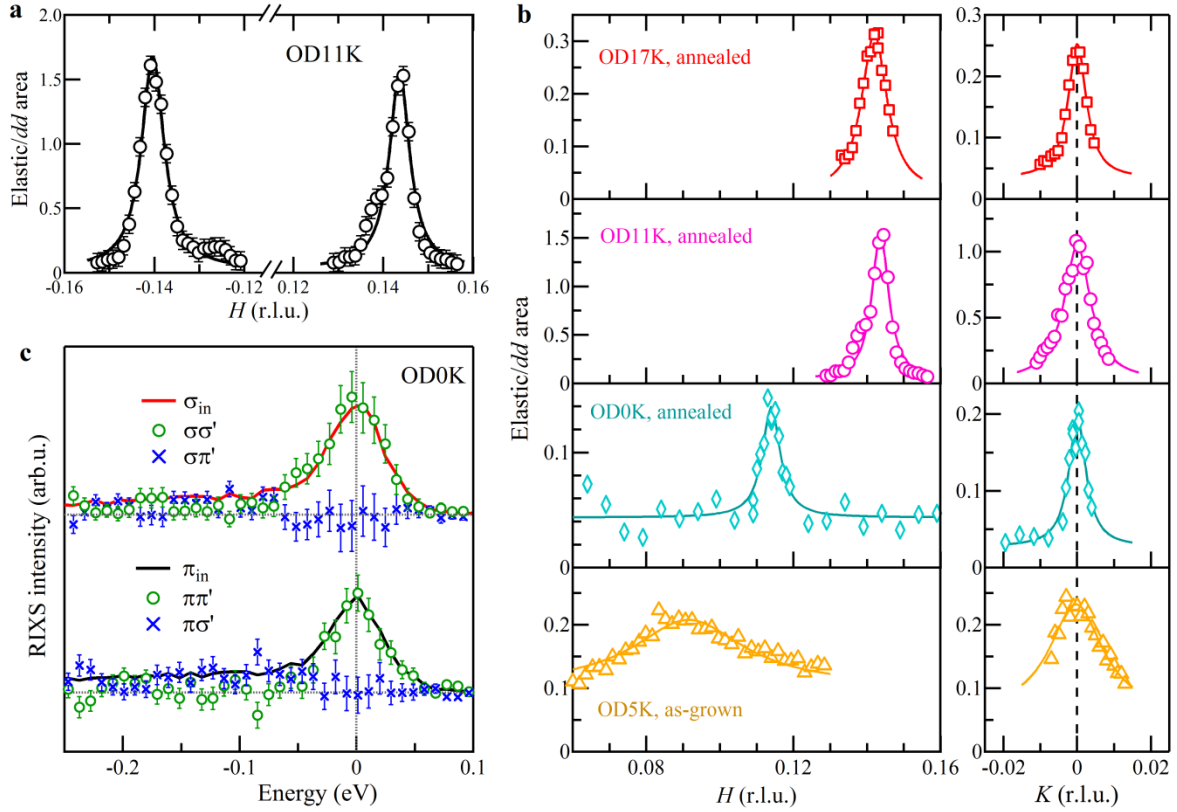


Figure 2: Doping and polarization dependence of the REXS peak in $(\text{Bi,Pb})_{2.12}\text{Sr}_{1.88}\text{CuO}_{6+\delta}$. **a**, REXS intensity for positive and negative H , using σ polarization. **b**, H and K cuts at 20K as indicated by the green cross in Fig. 1d, at 4 doping levels. Solid lines are Lorentzian peak fits to the data with a constant background. **c**, Polarization resolved measurements for OD0K ($p \approx 0.23$) taken at $H \approx 0.115$ r.l.u. with incident π - and σ -polarized light. Statistical error bars are calculated from the number of counts (see Supplementary Information).

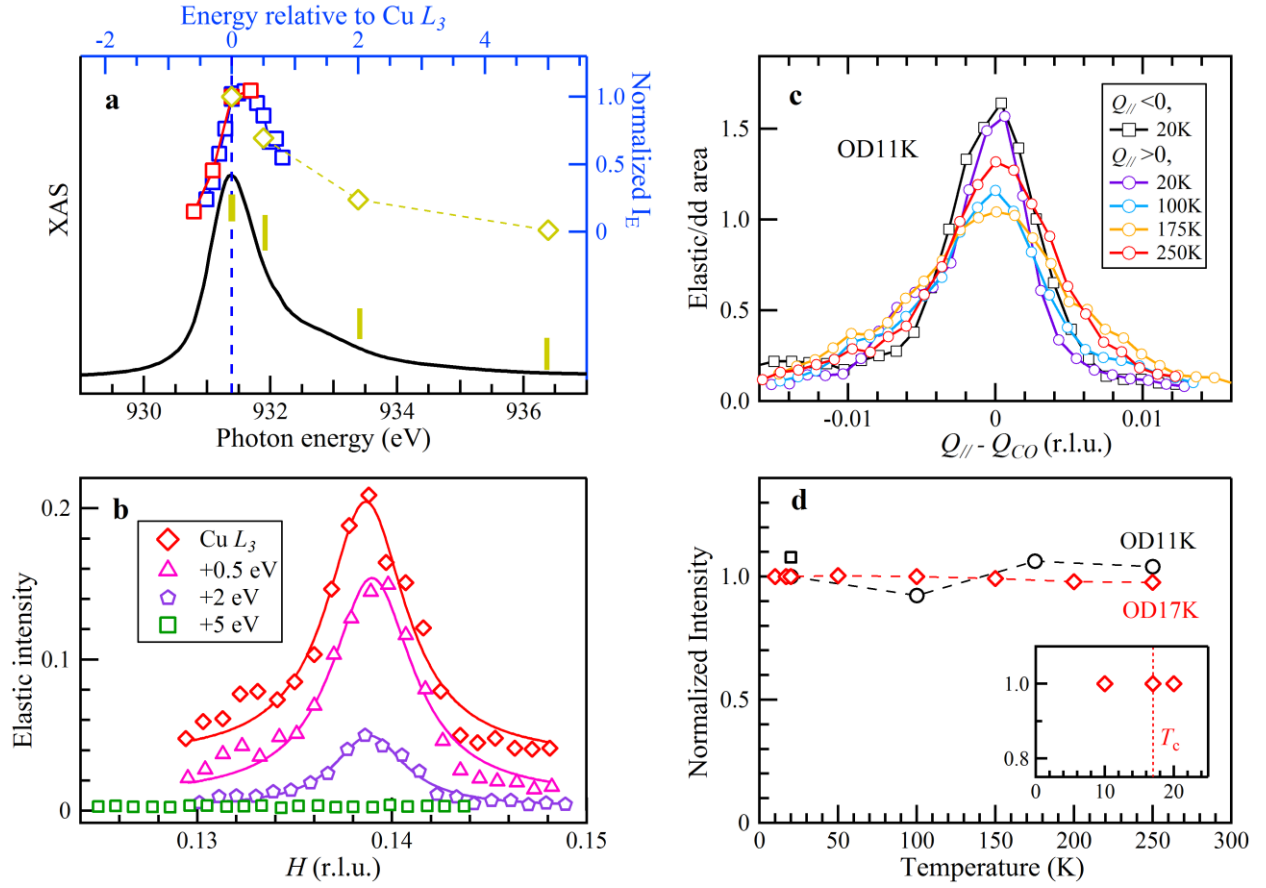


Figure 3: Energy and temperature dependence of the REXS peak in $(\text{Bi,Pb})_{2.12}\text{Sr}_{1.88}\text{CuO}_{6+\delta}$. **a**, (Left/Bottom) XAS spectra of OD17K with σ polarization at normal incidence. (Right/Top) Incident energy dependence of the REXS intensity, normalized to the value at XAS peak: hollow blue (red) squares for π (σ) polarization of OD11K, brown diamonds for σ polarization of OD17K. **b**, REXS scans along H direction for OD17K at 20K, at selected incident energies indicated by the brown lines in (a). Solid lines are Lorentzian peak fits to the data with a constant background. **c**, Comparison of REXS scans at selected temperatures for OD11K with $Q_{CO} \approx \pm 0.14 (\pm 0.005)$ r.l.u.. **d**, T -dependence of the charge order intensity in OD11K and OD17K, normalised to the value at 20K at $Q_{//} > 0$. The inset zooms in the low temperature region around T_c for OD17K.

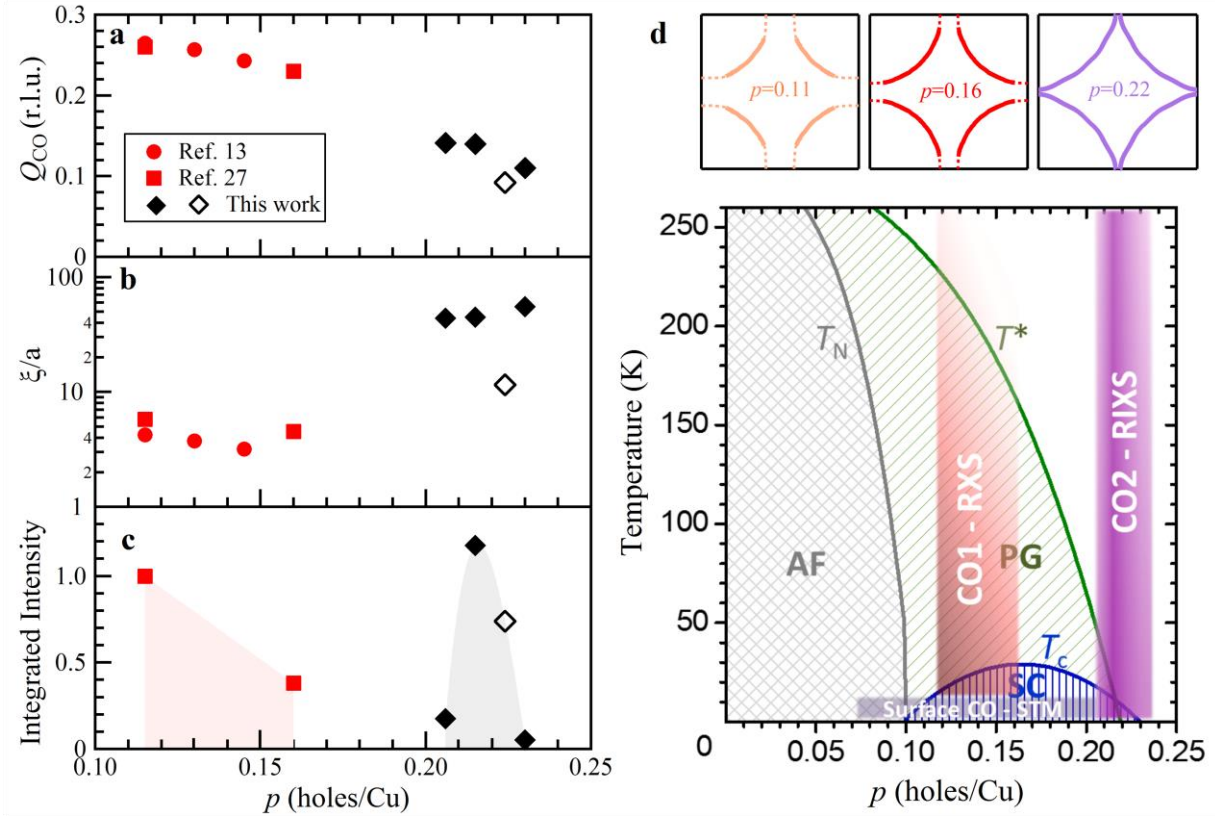


Figure 4: Doping dependence of the charge order signal in $(\text{Bi,Pb})_{2.12}\text{Sr}_{1.88}\text{CuO}_{6+\delta}$ and the corresponding phase diagram. a-c, Doping dependence of the CO wave vector, correlation length and the integrated intensity normalized to the value at $p \approx 0.115$. Data from RXS^{13,27} are included; black diamonds for annealed (solid) and as grown (hollow) samples. Error bars are smaller than symbol dimensions. d, The phase diagram of the charge order in Bi2201: it shows the antiferromagnetic region (AF) defined by T_N , superconducting region (SC) defined by T_c , and the pseudogap region (PG) defined by T^* , which are reproduced from NMR measurements³¹. The grey shaded area for the checkerboard charge order observed with STM from $p=0.07$ (ref. 36) to $p=0.21$ (ref. 37); the red shaded area for the CO measured with x-ray^{13,27}; the violet shaded area denotes the region of the newly discovered CO. The Fermi surfaces at selected doping $p=0.11$, 0.16 and 0.22 are schematically depicted on the top panels, breaking into Fermi arcs at $T < T^*$.